metals

MDPI

Article

Experimental and Numerical Investigation of Hot Extruded Inconel 718

Stefano Bacchetti [1], Michele A. Coppola [1], Francesco De Bona [2,*], Alex Lanzutti [2], Pierpaolo Miotti [1], Enrico Salvati [2] and Francesco Sordetti [2]

[1] Pietro Rosa TBM, 33085 Maniago, Italy; sbacchetti@pietrorosatbm.it (S.B.); mcoppola@pietrorosatbm.it (M.A.C.); pmiotti@pietrorosatbm.it (P.M.)
[2] Department Polytechnic of Engineering and Architecture, University of Udine, Via delle Scienze 208, 33100 Udine, Italy; alex.lanzutti@uniud.it (A.L.); enrico.salvati@uniud.it (E.S.); francesco.sordetti@uniud.it (F.S.)
* Correspondence: debona@uniud.it; Tel.: +39-0432558269

Abstract: Inconel 718 is a widely used superalloy, due to its unique corrosion resistance and mechanical strength properties at very high temperatures. Hot metal extrusion is the most widely used forming technique, if the manufacturing of slender components is required. As the current scientific literature does not comprehensively cover the fundamental aspects related to the process–structure relationships, in the present work, a combined numerical and experimental approach is employed. A finite element (FE) model was established to answer three key questions: (1) predicting the required extrusion force at different extrusion speeds; (2) evaluating the influence of the main processing parameters on the formation of surface cracks using the normalized Cockcroft Latham's (nCL) damage criterion; and (3) quantitatively assessing the amount of recrystallized microstructure through Avrami's equation. For the sake of modeling validation, several experimental investigations were carried out under different processing conditions. Particularly, it was found that the higher the initial temperature of the billet, the lower the extrusion force, although a trade-off must be sought to avoid the formation of surface cracks occurring at excessive temperatures, while limiting the required extrusion payload. The extrusion speed also plays a relevant role. Similarly to the role of the temperature, an optimal extrusion speed value must be identified to minimize the possibility of surface crack formation (high speeds) and to minimize the melting of intergranular niobium carbides (low speeds).

Keywords: extrusion; Inconel 718; metal-forming simulation

Citation: Bacchetti, S.; Coppola, M.A.; De Bona, F.; Lanzutti, A.; Miotti, P.; Salvati, E.; Sordetti, F. Experimental and Numerical Investigation of Hot Extruded Inconel 718. *Metals* **2023**, *13*, 1129. https://doi.org/10.3390/met13061129

Academic Editor: José Valdemar Fernandes

Received: 19 May 2023
Revised: 12 June 2023
Accepted: 13 June 2023
Published: 16 June 2023

1. Introduction

Inconel 718 is probably one of the most important among the nickel-based superalloys, due to its exceptional properties such as high oxidation resistance, corrosion resistance and high mechanical strength, even at high temperatures. For this reason, Inconel 718 is currently widely employed in the aircraft engine industry [1,2]. Specifically, it is used in many critical engine components (i.e., diffusers, combustion chambers, shells of gas generators, rocket engines and gas turbines), accounting for over 30% of the total finished component mass of a modern aircraft engine [3].

Despite its outstanding properties, the workability of Inconel 718 shows several unsolved critical issues. Its peculiar physics characteristics, such as its lower thermal conductivity, work hardening, presence of abrasive carbide particles, hardness, affinity for reacting with the tool material, etc., make Inconel 718 difficult to machine [4–6]. Recent advances in various material processing techniques, e.g., turning, milling and drilling, for machining Inconel 718 are investigated and discussed in [7]. Although Inconel 718 is supposed to possess good weldability, cracking problems may still arise [8,9]. As highlighted

in a welding process review [10], strain cracking during the post-weld heat treatment, solidification cracking and liquation cracking may still arise. In the last decade, the possibility to obtain Inconel 718 components by using additive manufacturing techniques was deeply explored [11]. In [12], Inconel 718 semi-finished parts were produced by selective laser melting (SLM) and tensile tests were performed, showing the capability of the SLM process to produce parts with mechanical properties better than forged and cast materials at room temperature and equal to properties to forged material at high temperatures. Recently, additively manufactured metamaterials were also obtained for the thermal stress accommodation of metal heat pipes [13]. Inconel 718 can be also coated to improve its wear resistance, as suggested in [14].

From the industrial end-user point of view, hot plastic deformation manufacturing processes remain the most common way to obtain Inconel 718 semi-finished parts. It is well-known that, in these cases, a detailed processing setup is mandatory to control recrystallization and grain growth phenomena. The main challenge during the hot working process of Inconel 718 is related to its high deformation resistance during forging and its tendency to form a duplex grain structure. These issues can be mitigated by precisely controlling both temperature and deformation during the manufacturing process [15]. As far as hot forging is concerned, a better understanding of the competition between several mechanisms (dynamic recovery, dynamic recrystallization and plasticity hardening) is presented in [16], where several thermo-mechanical parameters are taken into account. Additionally, an interesting study on the spatial microstructural evolution of the as-forged and heat-treated Inconel 718 disks can be found in the literature [17]. In this case, due to the different thermomechanical conditions across the thicknesses, a variation in the grain size and characteristics of the reinforcing precipitates were observed.

When the final product is characterized by a high aspect ratio, i.e., turbine blades, hot metal extrusion techniques are generally preferred. This process induces higher plastic deformation in comparison to forging, thus a finer process parameter tuning is required to avoid unwanted microstructural effects [18]. A typical failure occurring during hot metal extrusion is due to the formation of surface cracks. Such a phenomenon was widely investigated only in the case of aluminum alloy extrusion, where T-shape extrusion experiments were performed and compared with finite element (FE) simulation, in order to evaluate the possible predictive criteria to assess material recrystallization and surface crack formation [19].

Nevertheless, to the best of the authors' knowledge, no works seem to be available in the literature dealing with the prediction of the above-mentioned microstructural aspects in the hot extrusion process of Inconel 718 superalloy, along with other technological characteristics, such as determining the extrusion force, speed and temperature given the geometry of the mold. To tackle this outstanding problem, a FE-based numerical model of the extrusion process of an Inconel 718 component was devised. In parallel, a series of experimental tests were designed and carried out to examine the extrusion of pre-heated Inconel 718 billets, thus allowing for the comprehensive validation of the numerical model and respective results. The validated model was then used to perform parametric analyses in order to pinpoint ranges of processing conditions that avoid the formation of unwanted features.

2. Materials and Methods

To accomplish all the envisaged tasks, the study focuses on the hot extrusion of an axisymmetric-shaped component presenting a high aspect ratio (≅1:8). Therefore, both experimental and modeling activities were based upon this assumption. In this section, all the experimental and numerical details regarding the analyses of the present study are reported.

2.1. Extrusion Process Set-Up

The studied extrusion setup consists of three main parts, i.e., a mould, a punch and a processed material (billet), as illustrated in Figure 1. According to this figure, the billet shows a cylindrical shape at the beginning of the extrusion process (a), to turn into a nail-like shape at the end (b). It is important to point out that the billet initial diameter is slightly smaller than that of the accommodating mold. This implies that the punch compression against the billet produces a radial expansion of the billet in the initial stage of the process. At the stage when the material can no longer radially expand, then the material flows through the narrower section of the mold. The punch arrests prior to reaching its mechanical travel stop in order to obtain the head of the extruded piece.

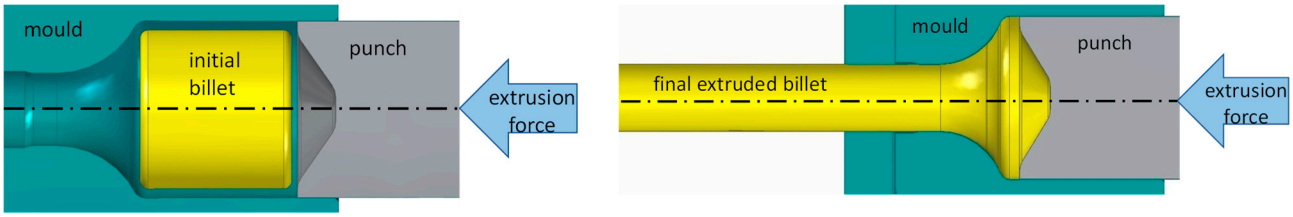

(**a**) (**b**)

Figure 1. Billet, mold and punch, respectively, (**a**) at the beginning and (**b**) at the end of the extrusion process.

2.2. Process Simulation and Material Modelling

At present, several commercial products are available for metal-forming simulation [20], based on FE approaches. The possibility of using a digital model, for the preliminary set-up of the technological process, would permit considerable time and cost reductions. Nevertheless, the reliability of these tools is still an object of debate, particularly concerning the material properties to be introduced in the model [21,22]. In the present work, Q-form (10.1.6 version) was used. A metal-forming process simulation of a structural component made of Inconel 718 can be found in the literature, using the same FE code [23]. Such a reference study presented a partial comparison with experiments, suggesting that the material model proposed herein is sufficiently accurate.

The simulation of hot plastic deformation processes generally requires huge computational time. In this case, an axisymmetric geometry was chosen, so that the dimension of the problem could be reduced by employing a plane model. The billet was modelled by 6-node triangular isoparametric elements (initial mesh: 9000 nodes, 17,000 elements). Generally, a plastic deformation process involves very high plastic strain, therefore, to avoid excessive element distortion, re-meshing was performed when strain increments higher than 0.1 among subsequent steps occurred. Moreover, the mesh was automatically updated where high strain and temperature gradients were detected. As the deformation of the mould is negligible, a fine mesh of this component was only required close to the inner surface where the thermal gradients could be relevant.

As the study is mainly related to the extrusion process simulation, the mold and punch were modelled as rigid bodies; their initial temperature was 200 °C and the initial temperature of the air was 20 °C. The dimension of the mesh was defined according to a sensitivity analysis performed referring to the damage parameter D.

The numerical model for the FE simulation is based on the usual flow formulation [24], where the material is considered as an incompressible rigid-viscoelastic continuum. The contact between the punch, mould and billet is dealt with according to a friction model proposed by [25]. It can be considered as a combination of constant friction and Coulomb friction models; the first one is dominant in the case of a high value of contact pressure, whereas, for low values, friction forces are approximately linearly dependent on the normal contact pressure.

The billet was made of Inconel 718, showing Ni (51.5%), Cr (18.4%), Fe (20%), Mo (3%) and Nb (5%) as major alloying elements (by weight %) with balanced other elements. The mold was made of a chromium-vanadium-molybdenum alloyed steel.

The physical and mechanical properties of the studied Inconel in the range 20–1100 °C were obtained from [26].

The flow stress of Inconel 718 at different strain rates and temperatures are reported for the case at ε = 0.7% in [27].

In a more general case, flow stresses can be obtained according to the following relations [28]:

$$\frac{\dot{\varepsilon}}{\bar{D}(T)} = A\left(sinh\alpha\frac{\sigma}{E(T)}\right)^{0.5} \quad (1)$$

where $\dot{\varepsilon}$ and σ are the strain rate and the flow stress, respectively, while $\bar{D}(T)$ is the self-diffusion coefficient, given by:

$$\bar{D}(T) = \bar{D}_0 exp\left(\frac{-Q_{st}}{RT}\right) \quad (2)$$

where R is the universal gas constant, T the absolute temperature, Q_{st} is the activation energy and $\bar{D}_0$ is the maximal diffusion coefficient. In the present study, the latter two constants are set as: $\bar{D}_0 = 1.6 \times 10^{-4}$ m^2/s and Q_{st} = 285 kJ/mol.

The dependence of the Young's modulus E to temperature T can be obtained through the following relation [29]:

$$E = 2(1+v)G \quad (3)$$

$$G = G_0\left(1 - 0.5\frac{v}{T_M}\right) \quad (4)$$

where G is the shear modulus, G_0 is the shear modulus at 300 K (8.31 $\times$ 10^4 MPa), T_M is the meeting temperature (1673 K) and v is the Poisson coefficient (0.33).

To predict the formation of surface cracks, a damage criterion can be adopted. Several fracture models are proposed in the literature. In [30], a thorough review of the most common ductile damage criteria is presented. Probably the most widely used phenomenological fracture model is the original Cockcroft Latham's criteria [31]. It assumes that the material fracture is controlled by maximum principal stress. This approach was improved in the normalized Cockcroft Latham's (nCL), also called Oh et al., a criterion where an equivalent stress is introduced to normalize the maximum principal stress. In the modified Cockcroft Latham's (called also Clift et al.) criterion, it is assumed that the ductile fracture starts or initiates when a critical value of plastic work per unit volume is achieved. Other fracture models (see [30] for more details), such as Mc Clintock's, Brozzo's and RT (also called Rice and Tracey) models, have been proposed and reported in the literature.

In [19,32], the nCL criterion was indicated as the best amongst the various existing criteria for the prediction of fracture initiation during extrusion. Recently, in [30], a comparative assessment of failure strain predictions using ductile damage criteria in the metal-forming of Inconel 718 was performed, concluding that the nCL criterion seems the most suitable option to predict fracture locus with high accuracy both at room and at high temperatures. The nCL was also adopted in [33], where a FE simulation of an Inconel 718 machining process was performed with the aim of predicting chip segmentation during orthogonal cutting. In particular, another study pointed out that the critical value of D in Equation (5) should be dependent on the strain path and, therefore, it cannot be considered as a material constant [34]. Thus, the nCL does not allow for a quantitative prediction of the damage for an arbitrary technological process of metal forming. The criterion can be used only for a qualitative comparison of similar technological processes. In this case, the nCL gives substantial support in evaluating the most critical zones of the final extruded component.

According to the previously mentioned literature assessments, in this work, the nCL damage criteria was used:

$$D = \int_0^{\bar{\varepsilon}_f} \frac{\sigma_I}{\sigma_{VM}} d\bar{\varepsilon} = \int_0^{t_f} \frac{\sigma_I}{\sigma_{VM}} \dot{\varepsilon} dt \quad (5)$$

where:

σ_I = maximum principal tensile stress;
$\bar{\varepsilon}_f$ = total equivalent strain;
σ_{VM} = von Mises equivalent stress;
$\dot{\varepsilon}$ = equivalent strain rate;
D = damage index.

The microstructure evolution can be simulated by means of a semi-empirical model [35]. The model takes into account both the recrystallization (dynamic and static) and grain growth, providing the average grain size and the fraction of recrystallized grains [36]. In the considered alloy, dynamic recrystallization usually occurs starting on deformed grain boundaries after the critical strain is reached for a certain applied strain at a certain processing temperature [37–39]. The fraction of recrystallized crystals X_{dyn} can be calculated by means of Equation (6). The formula is obtained from Avrami's equation:

$$X_{dyn} = 1 - exp\left[-ln2\left(\frac{\varepsilon}{\varepsilon_{0.5}}\right)^{1.9}\right] \quad (6)$$

The strain condition $\varepsilon_{0.5}$ at which 50% of grains are recrystallized (Equation (7)), that is a parameter necessary to determine the fraction of dynamically recrystallized grains, depends on the initial grain size d_0 and on the Zener–Hollomon parameter Z, which is calculated on the basis of processing conditions (strain rate and temperature).

$$\varepsilon_{0.5} = 0.029\, d_0^{0.2} Z^{0.06} \quad (7)$$

The grain size during dynamic recrystallization $\overline{\overline{D}}_{dyn}$ can be determined by Equation (8), which considers the Zener–Hollomon parameter as the most important to describe the grain size evolution:

$$\overline{\overline{D}}_{dyn} = 1.35 \cdot 10^3 d_0^{-0.01} \cdot Z^{-0.124} \quad (8)$$

Further recent work concerning the simulation of microstructure evolution and dynamic crystallization in hot plastic deformation of metals can be found in [40,41].

The main process parameters analyzed in the simulations are the punch speed and the initial temperature of the billet T_b in the range 1020–1090 °C, within the classic deformation temperature limits for Inconel 718 hot working [26]. In fact, these alloys are limited in terms of processing temperatures due to the intergranular precipitations of Nb compounds at temperatures above 1150 °C that reduce the ductility of the material, while, at temperatures below 950 °C, the material is prone to generate adiabatic shear bands [27].

The mold geometry is characterized by an extrusion ratio of ~1:6. The punch and mold undergo relevant loads during the extrusion process and, thus, they must be designed thoroughly, in order to avoid possible failures. Nevertheless, this aspect is strongly related to the specific product shape and thus it is not the objective of this work.

2.3. Extrusion Process Test

The parent billets were obtained by cutting a circular bar and turned to remove sharp edges, thus facilitating its self-centering at the first phase of the process. To lubricate and avoid oxidation at the surface of the billets, a glass-based coating was subsequently applied (see Figure 2a).

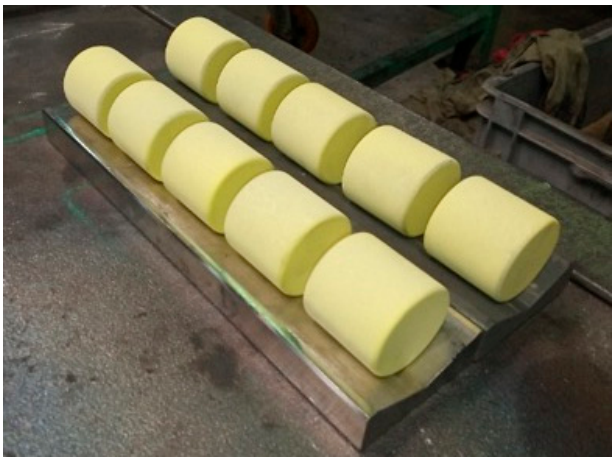

(**a**)

(**b**)

(**c**)

(**d**)

Figure 2. Set of glass-coated billets (**a**) ready for the extrusion test and (**b**) after the test. Surface crack formation after preliminary tests (**c**) and close up view (**d**) of the damaged zone.

To perform the extrusion tests, the following procedure was carried out:

- The billet was heated to a temperature T_b (holding time 1500 s).
- The punch and mold were lubricated with a graphite and water mixture.
- The billet was transferred from the oven to the mold (duration time: 3 s).
- The billet was maintained in position for 3 s (in this phase, heat was transferred from the billet to the mold)
- The punch was moved forward to perform the extrusion of the billet at constant speed v.
- Finally, the punch was retracted and the extruded billet was extracted.

A total of 63 tests were performed at different extrusion speeds, spanning from $0.27v_{max}$ to $1.0v_{max}$ and at an initial temperature of the billet of T_b = 1090 °C. v_{max} is a normalizing velocity. The selected speed range and temperature was set, such that the formation of surface cracks was inhibited. In particular, in the present study, higher temperatures (>1095 °C and lower extrusion speeds ($<0.270v_{max}$) were discarded as preliminary experimental tests showed the formation of surface cracks on final extruded components at $0.19v_{max}$ and at T = 1110 °C. An example is shown in Figure 2c,d.

The value of the force was obtained by measuring the hydraulic fluid pressure at a sampling speed of 100 Hz.

2.4. Macro and Micro-Structure Analysis

The extruded specimen underwent a macro- and micro-structural characterization. In particular, one extruded sample was cut into two halves along the longitudinal direction to obtain flat surfaces, above which the microstructural analyses were performed. The target surface was then manually ground and polished to obtain a mirror-like surface. Afterwards, the sample was macro-etched (submerged) by using a solution of HCl and iron chloride for

30 min. The sample was finally rinsed in deionized water with 1 M of sodium bicarbonate and visually inspected to analyze the macroscopic structural features.

Following this, metallographic samples were extracted from the previously analyzed sample at the areas circled in Figure 3. These samples were ground and polished again to reach a mirror-like surface and then etched using Marble's etchant for 1–2 min to reveal the microstructure. The microstructure was then analyzed by light microscopy and the grain size was measured through the line intercept method. The exact locations of analyses are indicated in Figure 3. In detail, the microstructural characterization was performed in the centerline of the test specimen and in the proximity of the extruded surface. The filleted region, indicated by the large circle in Figure 3, was analyzed in detail from a microstructural point of view in order to detect the critical deformation that triggers the grain crystallization. In this area, an evaluation of the recrystallized fraction was carried out by using the image analysis approach (phase partition analysis).

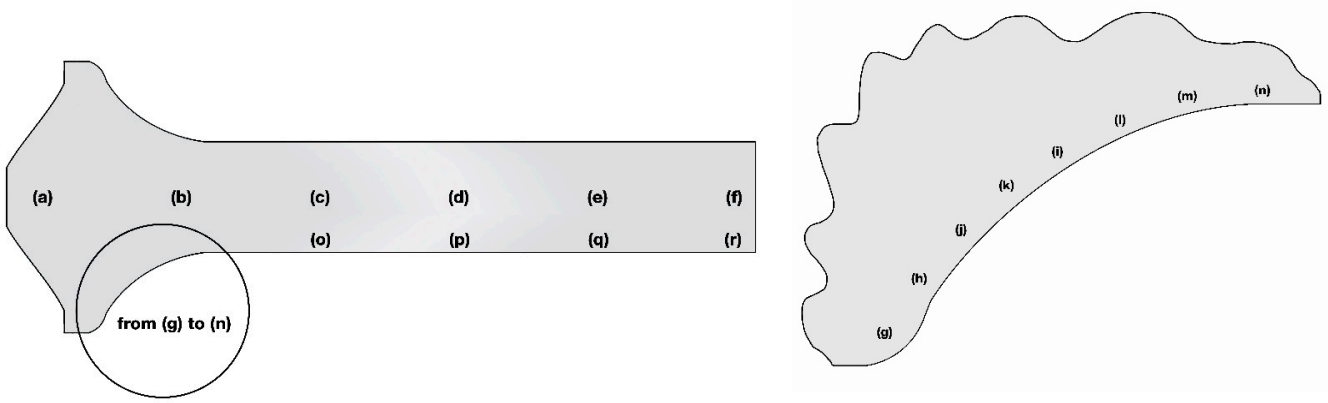

(**a**) (**b**)

Figure 3. Microstructural characterization map of analysis: (**a**) overall view of the component and (**b**) close up view of the fillet region.

3. Results and Discussion

3.1. Extrusion Process and Force Evolution: Numerical Simulation and Experiments

Thanks to the numerical simulation of the hot extrusion process, it is possible to graphically distinguish three phases of the process (see Figure 4), referring to an extrusion speed $v = 0.67v_{max}$. At t = 0, the punch touches the billet, producing its radial expansion up to t = 0.09 s. After that time, the material starts flowing inside the matrix up to t = 0.18 s. During this phase, the high friction between the billet and the mold produces heat and, consequently, a significant increase in the temperature of the billet. From t = 0.18 s up to the end of the process (t = 0.35 s), the billet shows its final forms and starts flowing more freely.

For the sake of the validation of the FE model, the extrusion force for two different extrusion speeds is compared (i.e., simulation vs. experiment). Figure 5 shows the evolution of the simulated extrusion force versus time for two different values of the extrusion speed. An interpretation of the force evolution can be proposed; during the first phase of the process (1), (see Figure 5), the slope of the curve is constant and relatively low, up to the beginning of the second phase (2), where a rapid increase is observed. This is mainly related to the large plastic deformation occurring in the billet. Moreover, the extrusion force has to overcome the high frictional forces due to the increase in the contact pressure occurring between the billet and the mold. In this phase, once the frictional force cannot increase any further, the peak force is reached. In the last phase (3), a slight decrease in the force is observed. This is due to the heat produced by the sliding of the mold with respect to the billet that increases the temperature of the material, thus reducing the flow stress. Moreover, as the extrusion process evolves, the contact between the extruded part and the mold shows a progressive area reduction at the head of the billet, with a consequent decrease in friction, thus a decrease in the extrusion force.

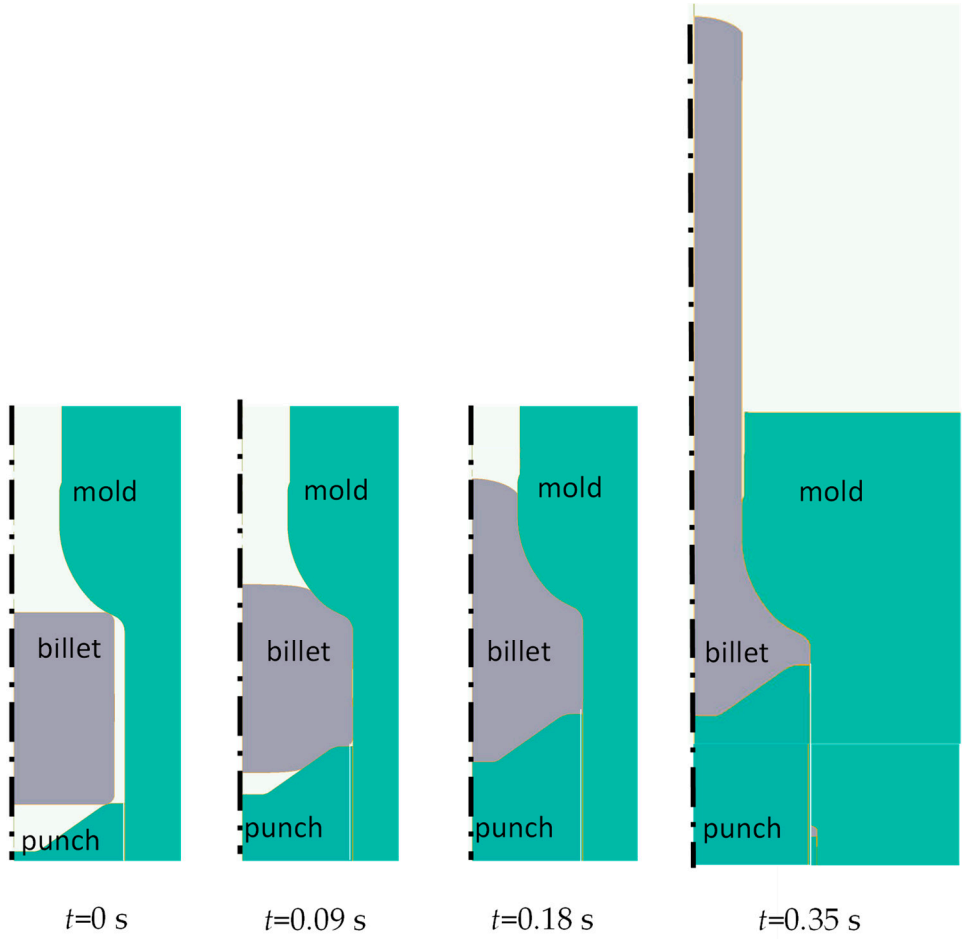

Figure 4. The three different phases of the process: simulated results.

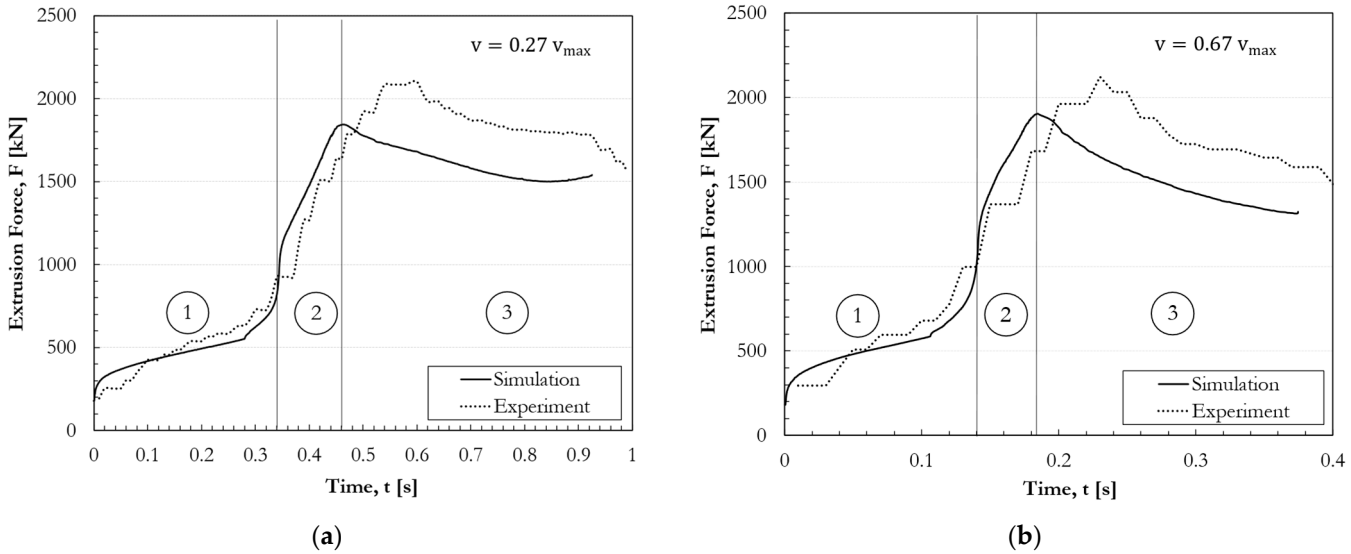

Figure 5. Extrusion force versus time for (**a**) an extrusion speed of $0.27v_{max}$ and (**b**) of $0.67v_{max}$.

The measured values of forces are also reported. The agreement is satisfactory in the first two extrusion phases (1 and 2, in Figure 5); in the third phase a higher difference is clearly observed. This is probably related to the high extrusion force reached in this phase. A large compression force thus acts on the punch, producing a radial expansion due to Poisson's effect. It follows that a slight shrink fit in the punch–mold coupling is likely to

arise. Therefore, an increase in the friction—and consequent force—takes place. In the simulation, the punch and mold were modeled as rigid bodies and, therefore, this effect could not be captured.

To even further support the validation concerning the extrusion force, a set of experiments and simulations were carried out at different extrusion speeds. Figure 6 shows the values of maximum extrusion forces (F_{max}) at different extrusion speeds; furthermore, the simulated results are compared with the experiments (each point is the average of 6–10 different tests). It can be observed that the extrusion force remains almost constant with respect to the extrusion speed. This is justified by considering that the increase in the flow stress (and also the force), with the strain rate (and the speed), is counterbalanced by the heat exchange from the billet to the mold that is reduced for high speeds, promoting high temperatures and subsequent low stress flow values. Simulated extrusion forces are always slightly lower with respect to the measurements; this is probably due to the uncertainty of the value of the friction parameters to be used in the simulation and also due to the shrink fit phenomena mentioned above.

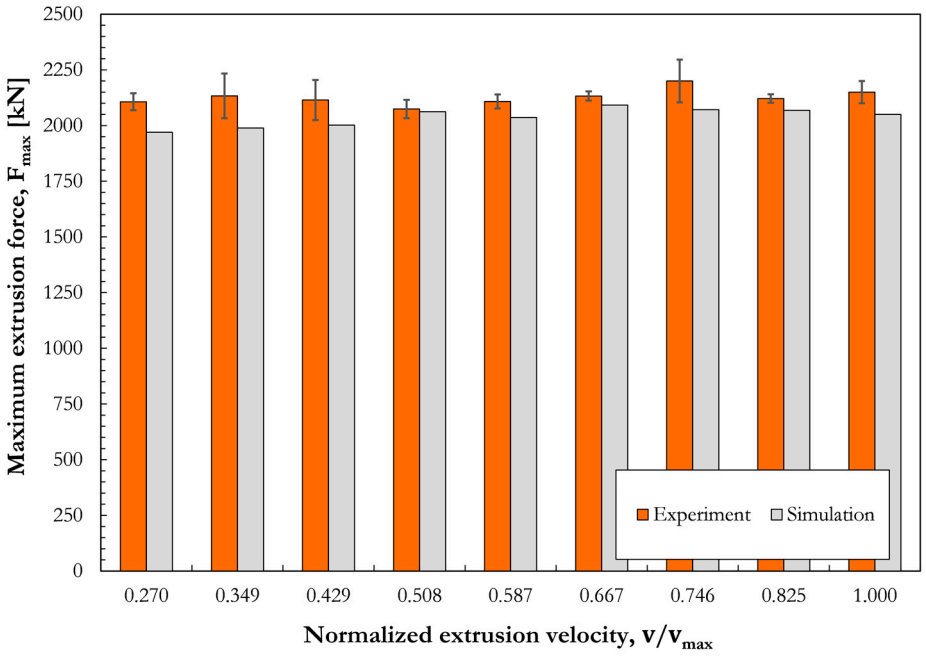

Figure 6. Maximum extrusion force for different extrusion speed: simulated and experimentally measured results.

3.2. Parametrical Analyses and Surface Crack Formation

In this section, the results of the parametric simulations to assess the influence of the billet temperature, and of the extrusion velocity, are shown.

Concerning the maximum extrusion force, Figure 7a shows its inverse proportionality to the initial billet temperature,T_b, at a constant extrusion speed of $0.67v_{max}$. This is due to the flow stress of the material that is higher at lower temperatures, making the extrusion force significantly increase. On the other hand, an increase in the D parameter also takes place when T_b increases, which nullifies the beneficial effect of the reduction in the extrusion force at higher T_b. Consequently, T_b must be chosen as the minimum temperature suitable to guarantee the extruded forces are compatible with the technological limits due to extruder payloads (T_b = 1090 °C in this case). Moreover, the influence of the extrusion speed on the maximum surface temperature T_b experienced at the surface of the billet and the damage parameter D are displayed in Figure 7b. Regarding the surface temperature, it is possible to observe its increase at high magnitudes of extrusion velocities. This can be imputed to the thermal exchange with the mold that is drastically reduced at high velocities and, thus, the process becomes almost adiabatic with a significant increase in

the billet temperature. Conversely, the greater the extrusion speed, the greater the damage parameter D. Nevertheless, as $T_{s,max}$ above 1150 °C has to be avoided, due to the possible intergranular melting of Niobium precipitates, extrusion speeds higher than 0.67 should be avoided.

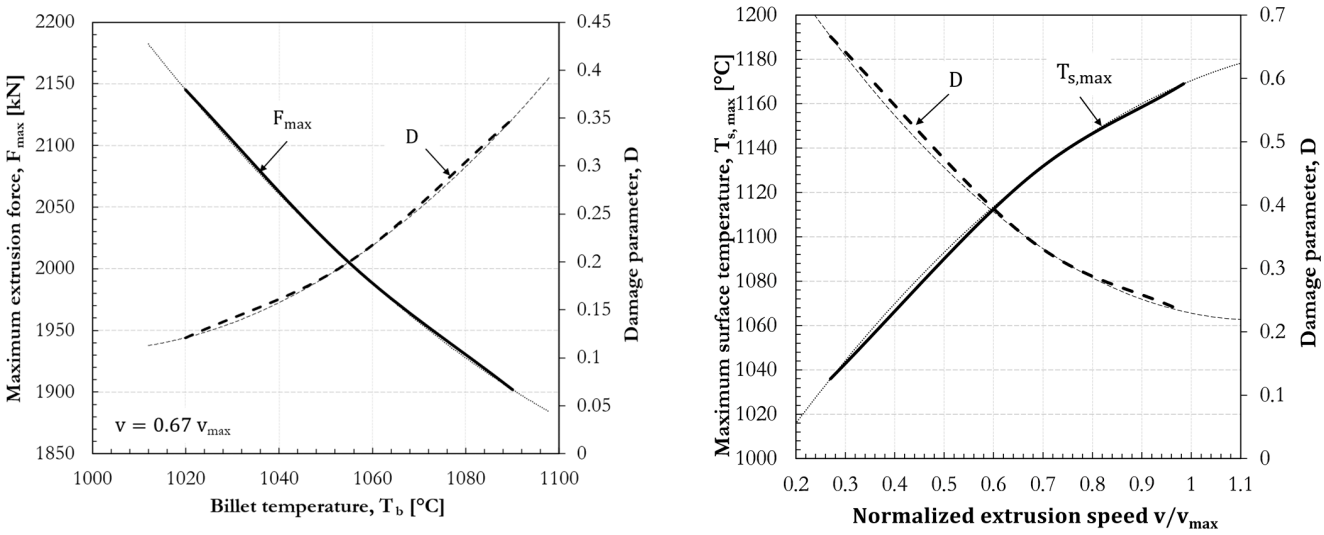

(**a**) (**b**)

Figure 7. Influence (**a**) of the initial billet temperature T_b on the maximum extrusion force and on the damage parameter D. Influence (**b**) of the normalized extrusion speed on the maximum surface temperature of the billet $T_{s,max}$ and on the damage parameter D.

For the sake of illustrating a significant full-field distribution of the damage parameter D over the analyzed domain, we decided to choose the following process parameters: T_b = 1090 °C and v = 0.67v_{max}. Following this, Figure 8 shows the result of this analysis. It can be observed that the most critical values occur over the surface of the upper part of the extruded workpiece (maximum value of D at the point labelled as "A"). In this zone, the risk of surface crack formation is higher than that of the remaining regions of the model. Although the damage parameter does not provide a quantitative evaluation of the crack formation condition, the proposed model is certainly capable of identifying the most critical regions, as verified by the preliminary experimental tests conducted in this work (see Figure 2c,d). Therefore, D should be minimized as much as possible to avoid material cracking within the limits of the other technological constraints.

In order to better understand the obtained results, point "A" was monitored throughout the whole extrusion process to observe the evolution of the damage parameter D (see Figure 9). It can be observed that ~50% of damage D accumulates during the first extrusion step that involves the billet expanding radially (1). At t = 0.08 s, the radial expansion of the billet in the mold is concluded and point "A" is located by the entrance of the mold diameter reduction. From t = 0.08 s to t = 0.18 s, mostly the inner part of the billet material starts to flow within the smaller section of the mold (2). In fact, in this time interval, point "A" does not undergo major displacement and deformation, therefore the damage parameter D remains almost constant. At t = 0.18 s, the severe plastic deformation of the flowing billet starts also involving the external regions of the billet, which slides with respect to the mold wall, including point "A". At t = 0.19 s, point "A" exits the mold and detaches from the mold wall (3). In this phase, a further increase in D occurs, mainly due to the positive stress in the axial direction induced by the friction forces and counterbalanced by the reaction of the mold. The evolution of the ratio $\frac{\sigma_I}{\sigma_{VM}}$ is also reported to be made clear, according to the expression reported in Equation (5), when the increase in D is related to an increase in the strain rate (1).

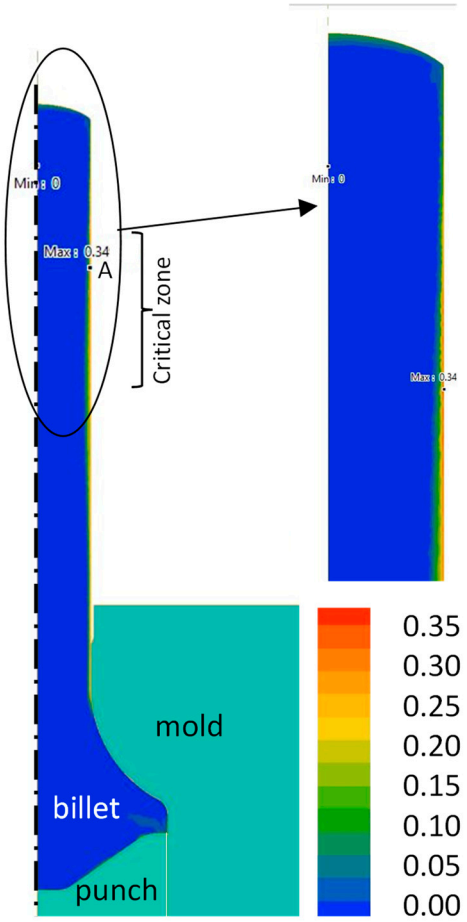

Figure 8. Contour plot of the damage parameter D over the billet at the end of the extrusion process for T_b = 1090 °C, $v = 0.67v_{max}$.

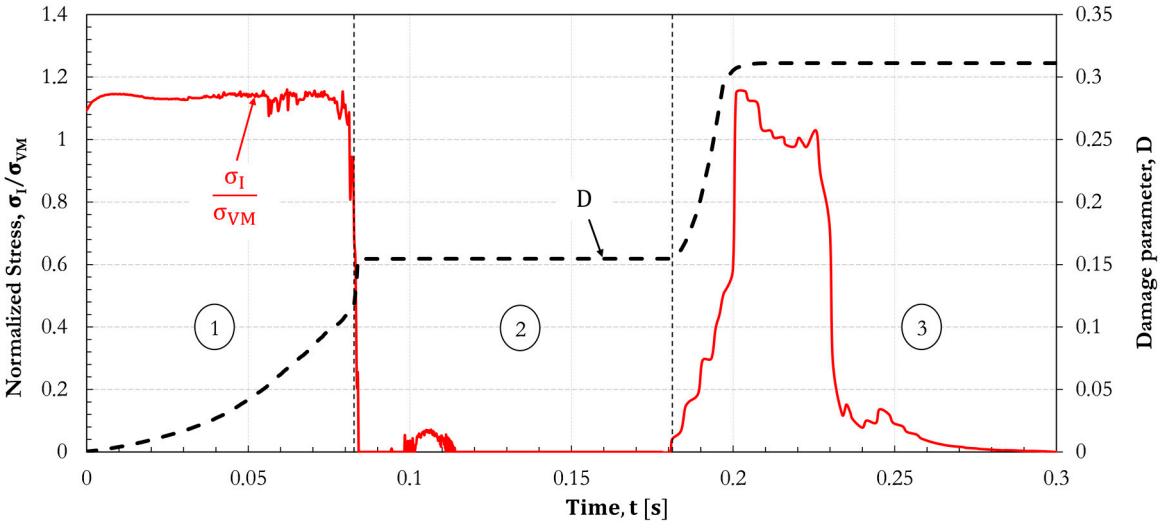

Figure 9. Evolution of the damage parameter D at point "A" during the extrusion process (T_b = 1090 °C) and of the ratio $\frac{\sigma_I}{\sigma_{VM}}$.

3.3. Experimental and Numerical Macro and Micro-Structure Analysis

The macro-etched sample (process parameters: T_b = 1090 °C; v = $0.67v_{max}$) shows the presence of a uniform microstructure along the main body of the billet (Figure 10). Some differences are well highlighted in the proximity of the ends of the extruded sample. In

detail, the two ends present a coarser grain distribution in comparison to the core of the billet. This grain distribution is linked to both low material deformation at the larger end, and at the material first undergoing extrusion at the thinner end. The extruded sample does not show any fibering due to both a possible homogenous chemical composition (absence of segregated areas) and to a probable homogenous monophasic recrystallized microstructure that is not prone to highlight the presence of microstructural bands.

Figure 10. Macro structure of the analyzed sample obtained after macro-etching.

The material, in any case, is composed of a monophasic gamma microstructure with no apparent precipitates at the micron-scale. Going into the details of the metallographic characterization, it is possible to observe a colony of grains along the centerline and close to the extruded free surface. In the centerline of the billet, the grain size is equiaxed and completely re-crystallized, although, in some regions, re-crystallization did not take place. The presence of these microstructural features probably indicates a meta-dynamic recrystallization process. No appreciable variations of the grain size were observed in the non-re-crystallized grains, although significant plastic deformation induced grain rotation and shearing effects. At the billet free-surface, the grains seem to be finer in comparison to the centerline due to higher cooling rates. Such experimental evidence allowed for the validation of the numerical model regarding the microstructure evolution, as shown in Figure 11. These results are in good agreement with the simulations in terms of the average grain size at the end of the process. In fact, finer grains can be easily observed at the extruded external surface with respect to the centerline, whereas, at the two ends, where the material is nearly undeformed, their dimension is unchanged (≅170 μm) in comparison to the pre-extrusion conditions.

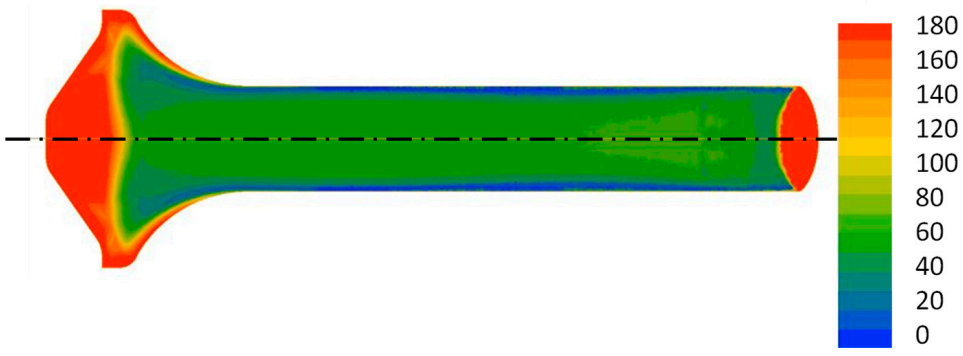

Figure 11. Average grain size (simulated) at the end of the process (in μm).

The analysis of the microstructure in the proximity of the billet large fillet in Figure 12 shows the presence of a gradual deformation of the grains leading to a re-crystallization of the material that is fully accomplished before the material flows outside the smaller section of the mold.

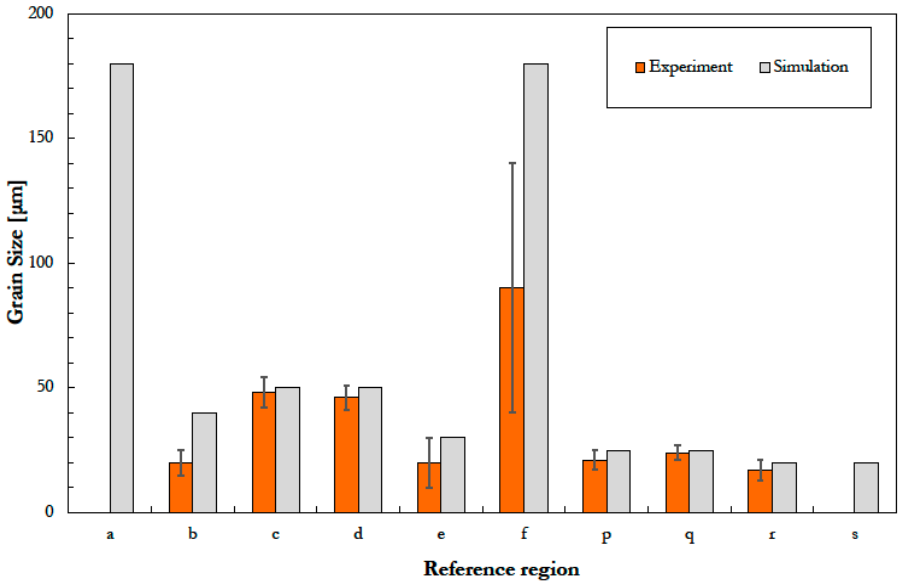

Figure 12. Grain size evaluation: experimentally measured vs. calculated. Labels refer to the regions listed in Figure 3. Note that regions (a) and (s) do not present a measured grain size.

A graph that compares the calculated grain dimension and the measured grain size is shown in Figure 12. The graph confirms that the regions with a fully recrystallized grain show a good agreement as far as the grain size is concerned, between the values evaluated by using the numerical methods previously presented and the experimental observations. On the other hand, the same match could not be fully verified at the regions where partial recrystallization occurred. In this case, the differences are more related to the difficulty in measuring the grain size by image analysis (intercept method).

Specifically, new grain nuclei, at approximately half of the fillet, are formed, where a mixture of re-crystallized and un-recrystallized grains are gradually observed. The position where around 50% of grains are recrystallized can be easily identified, and it corresponds, by comparing the position from microstructural characterization (Figure 13), to the plastic strain map obtained from the simulation (Figure 14), to a total strain between 1.2 and 1.5.

In this region, the plastic strains can also be experimentally evaluated by analyzing the length of undeformed grains and comparing this measurement to the initial dimension of the austenitic grain to assess the total strain in this position. A very good match was found with the total strain obtained from the numerical model.

Finally, the length of the extruded samples was measured and compared with the analogous dimensions obtained via simulation, observing a difference that was always lower that 5%. This value fulfills the technological requirements for the considered component.

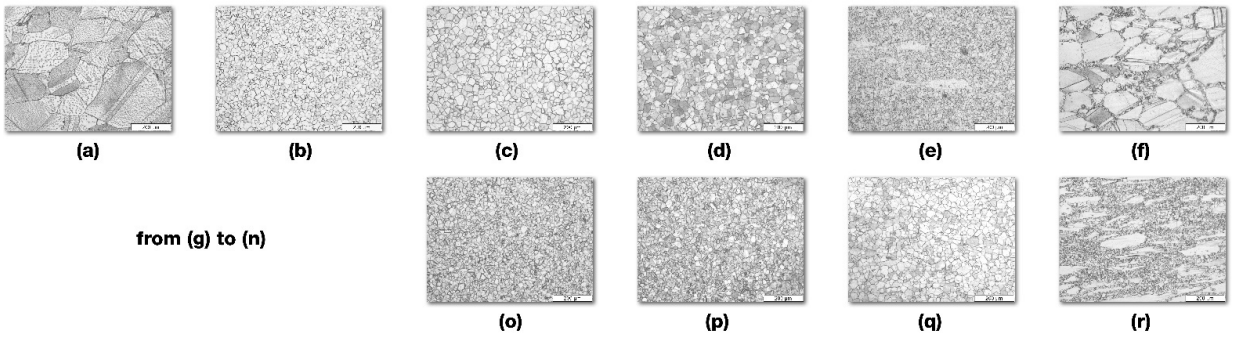

Figure 13. *Cont.*

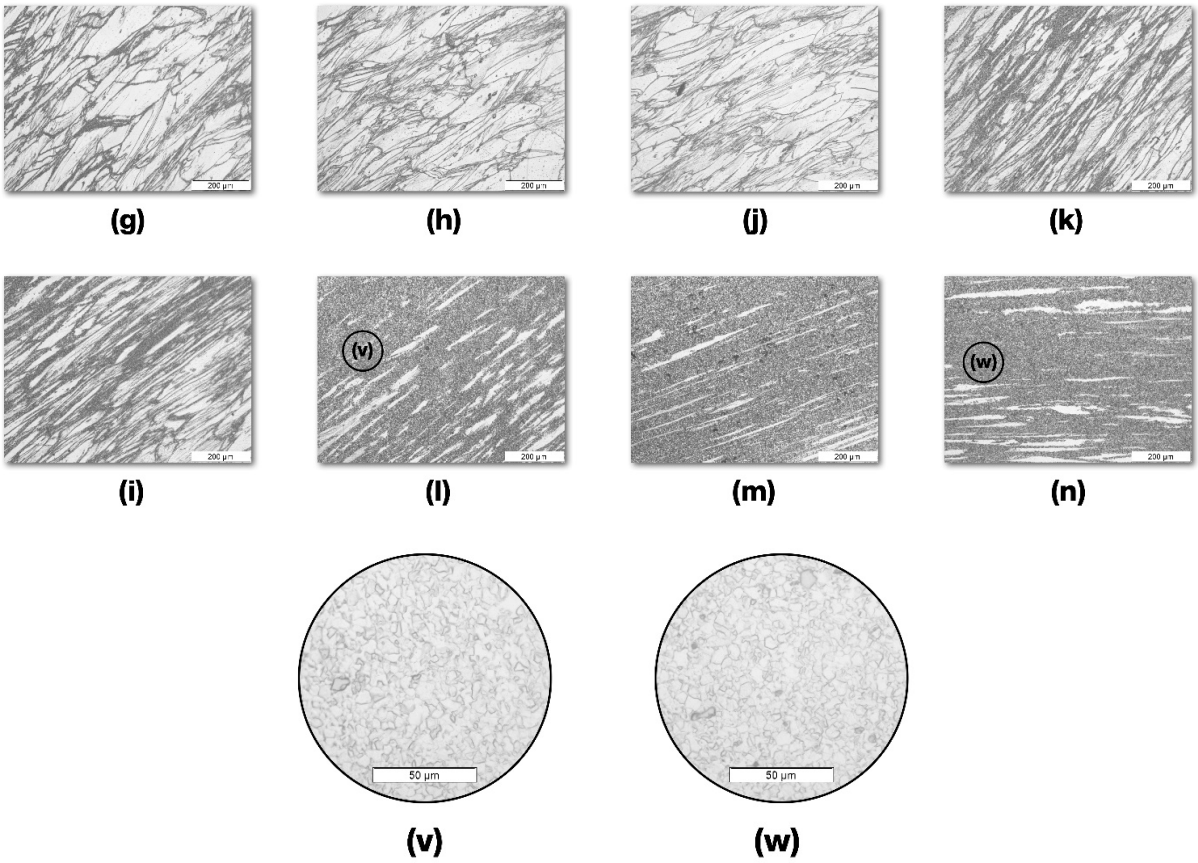

Figure 13. Microstructural characterizaion of the final billet (refer to Figure 3).

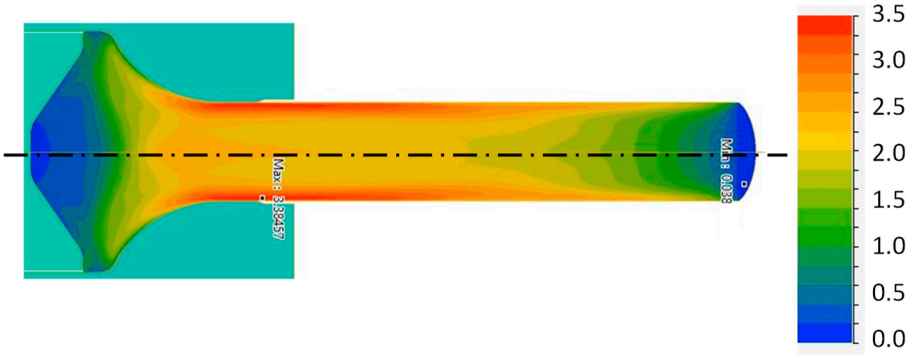

Figure 14. Strain distribution at the end of the extrusion process.

4. Conclusions

In this work, an extensive study was carried out to tackle the problem of Inconel 718 hot extrusion by employing both numerical and experimental methods, a subject that is scarcely addressed by the current literature. The development of a numerical approach, supported by experimental evidence, allowed for the evaluation of how key technological parameters (i.e., initial temperature of the billet, extrusion speed) affect both the required extrusion force and the final quality of the product (i.e., surface cracks, microstructure). The results show a very good agreement between the measurements and simulation. In particular, the proposed model was able to accurately predict the evolution of the extrusion force and the location of the zone of possible surface crack formation. Additionally, the model was capable of accurately capturing the microstructural grain deformation and re-crystallization.

Thanks to the fully validated developed model, the following recommendations can be drawn to attain the structural integrity and the sought mechanical performance of the final product. A higher initial temperature of the billet permits the extrusion force to be reduced, although the surface quality of the final product may be impaired if such a temperature is excessively increased. For the case presented in this work, a temperature around 1090 °C could be a reasonable trade-off. An increase in the punch speed is also advisable, as it lowers nCL's damage parameter, reducing the probability of surface cracks formation. Nevertheless, excessive values of speed could produce an increase in the temperature of the billet, which may be detrimental as it may induce the local melting of niobium carbide. An extrusion speed of $0.6 \div 0.7$ v/v_{max} could fulfill the abovementioned requirements.

The proposed procedure aims at providing a robust tool for the setting up of hot extrusion processes, regardless of the complexity of the geometry. This aspect is pivotal to reducing the design-to-market time and massively reduces the costly trial and error approaches.

Author Contributions: Conceptualization, P.M. and F.D.B.; methodology, S.B. and A.L.; software, M.A.C. and S.B.; validation, S.B. and A.L.; formal analysis, S.B. and F.S.; investigation, S.B. and A.L.; resources, F.S.; data curation, S.B.; writing—original draft preparation, F.D.B.; writing—review and editing, F.D.B. and E.S.; visualization, E.S.; supervision, F.D.B. and P.M.; All authors have read and agreed to the published version of the manuscript.

Funding: This research received no external funding.

Data Availability Statement: Restrictions apply to the availability of these data. Data were obtained from Pietro Rosa TBM and are available from the authors with the permission of Pietro Rosa TBM.

Conflicts of Interest: The authors declare no conflict of interest.

References

1. Salvati, E.; Lunt, A.J.G.; Ying, S.; Sui, T.; Zhang, H.J.; Heason, C.; Baxter, G.; Korsunsky, A.M. Eigenstrain reconstruction of residual strains in an additively manufactured and shot peened nickel superalloy compressor blade. *Comput. Methods Appl. Mech. Eng.* **2017**, *320*, 335–351. [CrossRef]
2. Tang, Y.T.; Panwisawas, C.; Jenkins, B.M.; Liu, J.; Shen, Z.; Salvati, E.; Reed, R.C. Multi-length-scale study on the heat treatment response to supersaturated nickel-based superalloys: Precipitation reactions and incipient recrystallisation. *Addit. Manuf.* **2023**, *62*, 103389. [CrossRef]
3. Qi, H. Review of inconel 718 alloy: Its history, properties, processing and developing substitutes. *J. Mater. Eng.* **2012**, *2*, 92–100.
4. Rahman, M.; Seah, W.K.H.; Teo, T.T. The machinability of Inconel 718. *J. Mater. Process. Technol.* **1997**, *63*, 199–204. [CrossRef]
5. Thakur, D.G.; Ramamoorthy, B.; Vijayaraghavan, L. Study on the machinability characteristics of superalloy Inconel 718 during high speed turning. *Mater. Des.* **2009**, *30*, 1718–1725. [CrossRef]
6. Felusiak-Czyryca, A.; Madajewski, M.; Twardowski, P.; Wiciak-Pikuła, M. Cutting forces during Inconel 718 orthogonal turn-milling. *Materials* **2021**, *14*, 6152. [CrossRef]
7. De Bartolomeis, A.; Newman, S.T.; Jawahir, I.S.; Biermann, D.; Shokrani, A. Future research directions in the machining of Inconel 718. *J. Mater. Process. Technol.* **2021**, *297*, 117260. [CrossRef]
8. Gordine, J. Some problems in welding Inconel 718. *WELD J.* **1971**, *50*, 480–484.
9. Chen, J.; Salvati, E.; Uzun, F.; Papadaki, C.; Wang, Z.; Everaerts, J.; Korsunsky, A.M. An experimental and numerical analysis of residual stresses in a TIG weldment of a single crystal nickel-base superalloy. *J. Manuf. Process.* **2020**, *53*, 190–200. [CrossRef]
10. Tharappel, J.T.; Babu, J. Welding processes for Inconel 718-A brief review. *IOP Conf. Ser. Mater. Sci. Eng.* **2018**, *330*, 012082. [CrossRef]
11. Salvati, E.; Lunt, A.J.; Heason, C.P.; Baxter, G.J.; Korsunsky, A.M. An analysis of fatigue failure mechanisms in an additively manufactured and shot peened IN 718 nickel superalloy. *Mater. Des.* **2020**, *191*, 108605. [CrossRef]
12. Trosch, T.; Strößner, J.; Völkl, R.; Glatzel, U. Microstructure and mechanical properties of selective laser melted Inconel 718 compared to forging and casting. *Mater. Lett.* **2016**, *164*, 428–431. [CrossRef]
13. Hu, L.; Shi, K.; Luo, X.; Yu, J.; Ai, B.; Liu, C. Application of additively manufactured pentamode metamaterials in sodium/Inconel 718 heat pipes. *Materials* **2021**, *14*, 3016. [CrossRef] [PubMed]
14. Wu, K.; Chee, S.W.; Sun, W.; Tan, A.W.-Y.; Tan, S.C.; Liu, E.; Zhou, W. Inconel 713C Coating by cold spray for surface enhancement of Inconel 718. *Metals* **2021**, *11*, 2048. [CrossRef]
15. Bauccio, M. *ASM Metals Handbook Vol. 14: Forming and Forging*, 9th ed.; ASM International: Tokyo, Japan, 1996.
16. De Jaeger, J.; Solas, D.; Baudin, T.; Fandeur, O.; Schmitt, J.H.; Rey, C. Inconel 718 single and multipass modelling of hot forging. In *Superalloys 2012: 12th International Symposium on Superalloys*; John Wiley & Sons Inc.: Chichester, UK, 2012; pp. 663–672.

17. Chamanfar, A.; Sarrat, L.; Jahazi, M.; Asadi, M.; Weck, A.; Koul, A.K. Microstructural characteristics of forged and heat treated Inconel-718 disks. *Mater. Des.* **2013**, *52*, 791–800. [CrossRef]
18. Jackman, L.A. Forming and Fabrication of Superalloys. In Proceedings of the Symposium on Properties of High Temperature Alloys, Las Vegas, NV, USA, 18–21 October 1976; pp. 42–58.
19. Duan, X.; Velay, X.; Sheppard, T. Application of finite element method in the hot extrusion of aluminium alloys. *Mater. Sci. Eng. A* **2004**, *369*, 66–75. [CrossRef]
20. Nielsen, C.V.; Martin, P.A.F. *Metal Forming: Formability, Simulation, and Tool Design*, 1st ed.; Academic Press: London, UK, 2021.
21. Moro, L.; Srnec Novak, J.; Benasciutti, D.; De Bona, F. Thermal distortion in copper moulds for continuous casting of steel: Numerical study on creep and plasticity effect. *Ironmak. Steelmak.* **2019**, *46*, 97–103. [CrossRef]
22. De Bona, F.; Novak, J.S.; Lanzutti, A.; Lucacci, G. Distortion after solubilization treatment of X12CrNiMoV12-3 beam-like samples: A novel FE modelling technique supported by experiments. *Eng. Fail. Anal.* **2022**, *135*, 106141. [CrossRef]
23. Biba, N.; Borowikow, A.; Wehage, D. Simulation of recrystallisation and grain size evolution in hot metal forming. *AIP Conf. Proc.* **2011**, *1353*, 127–132.
24. Zinkiewitcz, O.C. Flow formulation for numerical solution of metal forming processes. In *Numerical Analysis of Forming Processes*; Pittman, J.F.T., Zienkiewicz, O.C., Woof, R.D., Alexander, J.M., Eds.; Wiley: Chichester, UK, 1984; pp. 1–44.
25. Levanov, A.N.; Kolmogorov, V.L.; Burkin, S.P.; Kartak, B.R.; Ashpur Yu, V.; Spassky Yu, I. *Kontaktnoe Trenie v Protsessakh Obrabotki Metallov Davleniem (Contact Friction in Metal Forming Processes)*; Metallurgiya Publish: Moscow, Russia, 1976.
26. *ASM Handbook Vol. 2: Properties and Selection: Nonferrous Alloys and Special-Purpose Materials*; ASM International: Tokyo, Japan, 1990.
27. Sui, F.L.; Xu, L.X.; Chen, L.Q.; Liu, X.H. Processing map for hot working of Inconel 718 alloy. *J. Mater. Process. Technol.* **2011**, *211*, 433–440. [CrossRef]
28. Thomas, A.; El-Wahabi, M.; Cabrera, J.M.; Prado, J.M. High temperature deformation of Inconel 718. *J. Mater. Process. Technol.* **2006**, *177*, 469–472. [CrossRef]
29. Frost, H.J.; Ashby, M.F. *Deformation—Mechanism Maps. The Plasticity and Creep of Metals and Ceramics*; Pergamon Press: Oxford, UK, 1982; pp. 54–55.
30. Mahalle, G.; Kotkunde, N.; Gupta, A.K.; Singh, S.K. Comparative assessment of failure strain predictions using ductile damage criteria for warm stretch forming of IN718 alloy. *J. Mater. Form.* **2021**, *14*, 799–812. [CrossRef]
31. Cockcroft, M.G.; Latham, D.J. Ductility and the workability of metals. *J. Inst. Met.* **1968**, *96*, 33–39.
32. Clift, S.E.; Hartley, P.; Sturgess, C.E.N.; Rowe, G.W. Fracture prediction in plastic deformation processes. *Int. J. Mech. Sci.* **1990**, *32*, 1–17. [CrossRef]
33. Jafarian, F.; Ciaran, M.I.; Umbrello, D.; Arrazola, P.J.; Filice, L.; Amirabadi, H. Finite element simulation of machining Inconel 718 alloy including microstructure changes. *Int. J. Mech. Sci.* **2014**, *88*, 110–121. [CrossRef]
34. Stebunov, S.; Vlasov, A.; Biba, N. Prediction of fracture in cold forging with modified Cockcroft-Latham criterion. *Procedia Manuf.* **2018**, *15*, 519–526. [CrossRef]
35. Sellars, C.M.; Whiteman, J.A. Recrystallization and grain growth in hot rolling. *Met. Sci.* **1979**, *13*, 187–194. [CrossRef]
36. Biba, N.; Stebunov, S.; Vlasov, A. Material forming simulation environment based on QForm3D software system. *Energy* **2017**, *2*, 4.
37. Na, Y.S.; Yeom, J.T.; Park, N.K.; Lee, J.Y. Prediction of microstructure evolution during high temperature blade forging of a Ni−Fe based superalloy 718. *Met. Mater. Int.* **2003**, *9*, 15–19. [CrossRef]
38. Gruber, C.; Raninger, P.; Stanojevic, A.; Godor, F.; Rath, M.; Kozeschnik, E.; Stockinger, M. Simulation of dynamic and meta-dynamic recrystallization behavior of forged alloy 718 Parts using a multi-class grain size model. *Materials* **2021**, *14*, 111. [CrossRef]
39. Soufian, E.; Darabi, R.; Abouridouane, M.; Reis, A.; Bergs, T. Numerical predictions of orthogonal cutting–induced residual stress of super alloy Inconel 718 considering dynamic recrystallization. *Int. J. Adv. Manuf. Technol.* **2022**, *122*, 601–617. [CrossRef]
40. Churyumov, A.Y.; Pozdniakov, A.V. Simulation of microstructure evolution in metal materials under hot plastic deformation and heat treatment. *Phys. Metals Metallogr.* **2020**, *121*, 1064–1086. [CrossRef]
41. Churyumov, A.Y.; Pozdnyakov, A.V.; Churyumova, T.A.; Cheverikin, V.V. Hot plastic deformation of heat-resistant austenitic aisi 310s steel. Part 1. simulation of flow stress and dynamic recrystallization. *Chernye Met.* **2020**, *9*, 48–55.